THESIS FOR THE DEGREE OF LICENTIATE OF ENGINEERING
IN SOLID AND STRUCTURAL MECHANICS

Modeling of Intraluminal Surfaces of Thoracic Aortas

JOHAN BONDESSON

Department of Mechanics and Maritime Sciences
Division of Dynamics
CHALMERS UNIVERSITY OF TECHNOLOGY

Gothenburg, Sweden 2020

Modeling of Intraluminal Surfaces of Thoracic Aortas
JOHAN BONDESSON

Licentiate thesis no. 2020:5
Department of Mechanics and Maritime Sciences
Division of Dynamics
Chalmers University of Technology
SE-412 96 Gothenburg
Sweden
Telephone: +46 (0)31-772 1000

Cover:
Figure is displaying the computational grid for a patient specific thoracic aorta along with longitudinal surface curvature distribution along inner, center, and outer lines, respectively. Dark red indicates the highest local curvature and dark blue the lowest.

Chalmers Digitaltryck
Gothenburg, Sweden 2020

Modeling of Intraluminal Surfaces of Thoracic Aortas
JOHAN BONDESSON
Department of Mechanics and Maritime Sciences
Division of Dynamics
Chalmers University of Technology

Abstract

Vascular diseases are getting more and more common as a result of modern-day lifestyle and the fact that the population is getting older. One of the newest treatments for vascular diseases such as aneurysms and dissections is endovascular repair with endografting. This treatment uses a fabric covered metallic structure that is implanted using a minimally invasive approach to serve as an artificial vessel in a damaged region. To ensure that the interventions are successful, the endograft must be placed in the correct location, and be designed to sustain the hostile biological, chemical, and mechanical conditions in the body for many years.

To accurately describe the complex mechanical conditions of the intraluminal surfaces of diseased blood vessels inside the body, this thesis presented a segmentation and quantification methodology for a natural and intuitive vessel surface description. The thesis also included some important clinical applications, all based on non-invasive temporal imaging. The results emphasized the need for explicit surface curvature quantification, as compared to relying solely on centerline curvature and estimation methods. Methods for preoperative prediction of endograft malapposition severity based on geometric analysis of thoracic aortic surfaces were introduced. Finally, a multiaxial dynamic analysis of cardiac induced thoracic aortic surface deformation showed how a thoracic endovascular aortic repair is affecting the deformations of the thoracic aorta.

Thus, the work presented in this thesis contributes by giving surgeons a tool to use in their treatment planning to minimize complications. Moreover, this method provides more nuanced boundary conditions so that endograft manufacturers can improve their designs to improve the quality of life for the treated patients.

Keywords: Thoracic aorta, aneurysm, dissection, geometric modeling, stereolithographic surface, surface curvature, TEVAR, endograft, bird-beaking, cardiac pulsatility

Preface

The work presented in this thesis was carried out from fall of 2017 to fall of 2019 at the Division of Dynamics, Department of Mechanics and Maritime Sciences, Chalmers University of Technology, and during a handful of visits to the Vascular Intervention Biomechanics & Engineering Laboratory (VIBE-lab) at Division of Vascular Surgery, Department of Surgery, Stanford University, California, Unitied States of America.

Acknowledgements

I want to thank everyone who have contributed to my research project, which ultimately have resulted in this thesis. Chris Cheng, for your excellent mentorship, Kelly Suh for your invaluable guidance, Michael Dake and Jason Lee for your clinical expertise, Torbjörn Lundh for introducing me to the field, and Mikael Enelund for taking me in as a PhD-student. I feel like we have just scratched the surface so far, and with your continued support, I am certain that the downstream projects will be yet more interesting and meaningful.

Next, I want to direct my appreciation to my family and friends in Sweden for your support, and Marc and Julia Zafferano for your hospitality when I have visited California. To have all of you in my life is a true blessing and I am grateful that you have been, and will continue to be, an integral part of my journey.

I also want to take the opportunity to thank the Barbro Osher Endowment for their financial support related to my research visit to Stanford during the fall of 2019.

Finally, I want to thank everyone who have doubted, questioned or challenged my decisions — you have made me even more determined to go my own way. Please continue to do so.

Göteborg, February 2020
Johan Bondesson

Thesis

This thesis consists of an extended summary and the following appended papers:

Paper A Johan Bondesson, Ga-Young Suh, Torbjörn Lundh, Jason T. Lee, Michael D. Dake, and Christopher P. Cheng. "Automated Quantification of Diseased Thoracic Aortic Longitudinal Centerline and Surface Curvatures". *Journal of Biomechanical Engineering* 142.4 (2020). DOI:10.1115/1.4045271

Paper B Maxfield M. Frohlich, Ga-Young Suh, Johan Bondesson, Jason T. Lee,Michael D. Dake, Matthew Leineweber, and Christopher P. Cheng. "Thoracic Aortic Geometry Correlates with Endograft Bird-beaking Severity". *Journal of Vascular Surgery* (in press, published online Feb 5, 2020). DOI:10.1016/j.jvs.2019.11.045

Paper C Ga-Young Suh, Johan Bondesson, John Kim, Yufei D. Zhu, Jason T. Lee,Michael D. Dake, and Christopher P. Cheng. "Biomechanical Effects of TEVAR on Multiaxial Pulsatility and Surface Curvature Deformation of the Thoracic Aorta". *To be submitted for publication*

Paper A: Johan Bondesson lead the project (methods development, validation, implementation and application on patient data) based on approaches discussed with Ga-Young Suh, Torbjörn Lundh and Christopher P. Cheng. Jason T. Lee and Michael D. Dake treated the patients. Johan Bondesson wrote the manuscript under the supervision of Christopher P. Cheng and all authors contributed in the process of proof-reading. Prior to journal submission, the work was presented at the Leipzig Interventional Course (LINC) in 2018: https://linc2018.cncptdlx.com/media/125.pdf.

Paper B: Maxfield M. Frohlich lead the project and wrote the paper in collaboration with Ga-Young Suh under supervision of Christopher P. Cheng and Matthew Leineweber. Johan Bondesson contributed to analysis and interpretation. Jason T. Lee and Michael D. Dake treated the patients. All authors contributed in the process of proof-reading. Prior to journal submission, the work was presented at LINC in 2018: https://linc2018.cncptdlx.com/media/124.pdf.

Paper C: Ga-Young Suh was the main responsible for this project. Johan Bondesson contributed with methods development and simulation, as well as writing parts of the manuscript. Jason T. Lee and Michael D. Dake treated the patients. John Kim and Yufei D. Zhu preformed modeling of patient data. All authors contributed in the process of proof-reading. Prior to journal submission, the work was presented at LINC in 2018: https://linc2018.cncptdlx.com/media/137.pdf.

The project was presented at the Svenska Mekanikdagarna in June 2019 at the Royal Institute of Technology, Stockholm, Sweden. Extended abstract found on page 23 in: https://www.kth.se/polopoly_fs/1.913522.1561399182!/SMD_2019_Program_Website.pdf

Contents

Abstract i

Preface iii

Acknowledgements iii

Thesis v

Contents vii

I Extended Summary 1

1 Background 1
1.1 Introduction . . . 1
1.1.1 Purpose and Aims . . . 2
1.1.2 Limitations . . . 3
1.2 Anatomy, Pathology, and Interventions . . . 4
1.2.1 Thoracic Aortic Anatomy . . . 4
1.2.2 Thoracic Aortic Pathology . . . 5
1.2.3 Endovascular Interventions and Devices . . . 5

2 Modeling of Aortic Surfaces 7
2.1 Imaging and modeling . . . 7
2.2 Segmentation . . . 8
2.3 Lagrangian Formulation . . . 9

3 Applications 11
3.1 Surface Curvature . . . 11
3.2 Endograft Malapposition Prediction . . . 12
3.3 Multiaxial Deformation Changes Due to TEVAR . . . 14

4 Summary of Appended Papers 15

5 Concluding Remarks and Future Work 17
5.1 Conclusions . . . 17
5.2 Future Work and Preliminary Results . . . 17

References 20

II Appended Papers A-C 23

Part I
Extended Summary

1 Background

1.1 Introduction

As reported by the World Health Organization, cardiovascular diseases are the leading cause of death globally, accounting for more than a third of all deaths each year [1]. A subset of these diseases is vascular diseases. This thesis focuses on two of them, namely *thoracic aortic aneurysms* and *thoracic aortic dissections*. Disease pathology and pathophysiology will be elaborated on more in Section 1.2.2. One treatment option for these diseases is a Thoracic Endovascular Aortic Repair (TEVAR), which involves one or multiple implants in the vascular system. These implants are referred to as *stent grafts* or *endografts*. However, there are several aspects that highly influences the outcome of the intervention, and among these, that the implant is correctly sized and placed, and that the long term integrity of the structure is secured. Incorrect placement or oversizing of the endograft can lead to complications such as:

- Malappositon of the endograft at the distal landing zone, also called *bird-beaking* because of the wedge shape created at the inner curve, as seen in Figure 1.1a [2].
- Unintended leakage of blood through or around the endograft; *endoleaks* [3].
- Migration of the endograft. This occurs when the device is moved from its intended placement, due to movement and hemodynamic forces. Oversizing can be an important factor for this type of complication [4].
- Device collapse due to in-folding of the distal end of a malapposed endograft [5].
- Device component failure. This is when one or several components of the endograft fractures. Note that component failure is only equal to a clinically relevant failure if enough components breaks for the device to collapse under the radial forces [6].

The other aspect, the long term structural integrity of the endograft, is dependent on myriad of factors (chemical, biological, and mechanical) and can cause material failure. Cyclic multiaxial loading of the vessels and implants due to cardiac and respiratory motion can cause fatigue damage to the implants, which can lead to component failure, see Figure 1.1b and 1.1c [7]. As mentioned previously, a component failure is not equal to a total failure, and failure of different components may cause different complications. For example, fracture of one strut of the stent may have no clinical complications (but fracture in several may cause the endograft to malperform), or wear-damage of the graft material may cause endoleaks. Here, it is crucial to rely on realistic boundary conditions derived from the movement of the vascular system in order to make durable device designs.

Ever since x-ray was invented, non-invasive tools for diagnosis and treatment support have grown increasingly advanced. Today imaging systems are fundamental tools before,

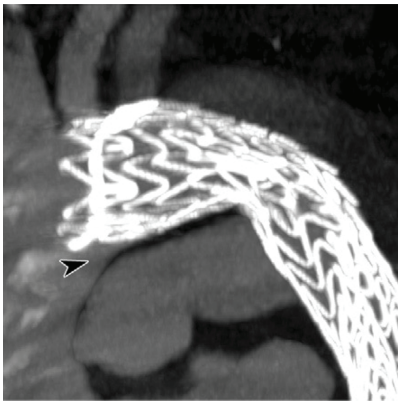

(a) An x-ray image showing the occurence of bird-beaking after TEVAR, Figure from [2].

(b) A close-up of a cross section of broken Nitinol stent component due to fatigue damage, Figure from [7].

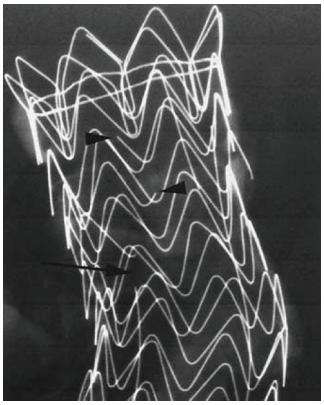

(c) A figure showing an endograft with multiple stent fractures, Figure from [7].

Figure 1.1: Figure showing examples consequences of bad device placement (bird-beaking), and inadequate design regarding durability (single strut failure, and multiple strut failures).

during and after interventions. In a strive to provide tools for a high-resolution description of the complex dynamics of the intraluminal surfaces of blood vessels, semi-manual modeling can be performed directly from 3D imaging data. Fully automatic segmentation algorithms based on artificial intelligence and machine learning are emerging. However, it will probably take years before they can reliably and accurately be used to replace the semi-manual methods used in this thesis. The higher level of fidelity is crucial for dynamic studies since the movements, and deformations, can be very small. With this said, it is today motivated to perform the tedious process of manual modeling. Previous work describing vessel motion has been largely focused on centerline and cross-sectional changes of the thoracic aorta [6]. However, since the endografts *in situ* in fact are located directly at the intraluminal vessel surfaces, there is a need to describe these surfaces explicitly with high accuracy.

1.1.1 Purpose and Aims

The purpose of this thesis can be divided into two: supporting clinicians in their treatment planning (choosing of devices and device placement), and providing medical device manufacturers with more realistic boundary conditions to assist design improvements. This purpose can be fulfilled through mechanical modeling as well as methodology development and validation to better describe the intraluminal surfaces of thoracic aortas. By doing so, anatomy, physiology, pathology, and pathophysiology can be better described and understood, both mechanically and clinically. An overview of how the modeling ties to the purpose is seen in Figure 1.2. Breaking down the purpose for this specific project, the following aims are formulated:

- Development of an automatic segmentation algorithm to quantify time-varying thoracic surface quantities, and after validation on phantoms, analyze patient

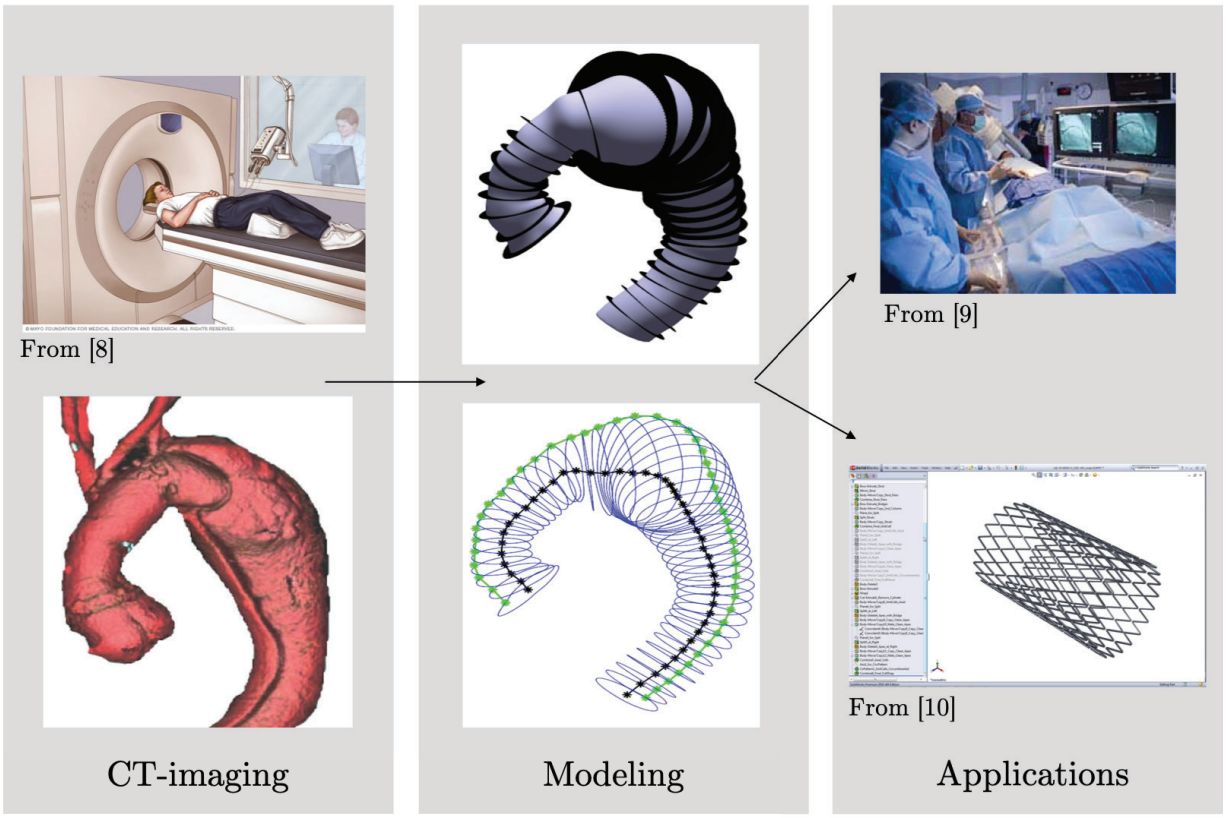

Figure 1.2: Figure showing the overall workflow from imaging, via modeling and surface description, to use as a pre- or intraoperative tool for clinicians, and boundary condition for device designers, respectively. Top left, top right, and bottom right are from [8], [9], and [10], respectively, whereas the other figures are from **paper A**.

specific geometries. This part is presented in **Paper A** with the application on longitudinal surface curvature for static cases.

- Investigation if endograft malappositon can be predicted preoperatively by building on the developed method mentioned. This application is described in **Paper B**.
- Study how endografts and TEVAR influences vessel compliance. This is presented in **Paper C**.

Figure 1.3 visualizes how the research papers in this thesis are connected.

1.1.2 Limitations

The scope of this thesis is limited according to the following list:

- The vessel segment studied is exclusively the thoracic aorta.
- Only two types of pathologies of the thoracic aorta are considered: aneurysms and dissections.
- Among treatment options, only TEVAR is considered when studying morphological and dynamic changes of the thoracic aorta due to interventions.

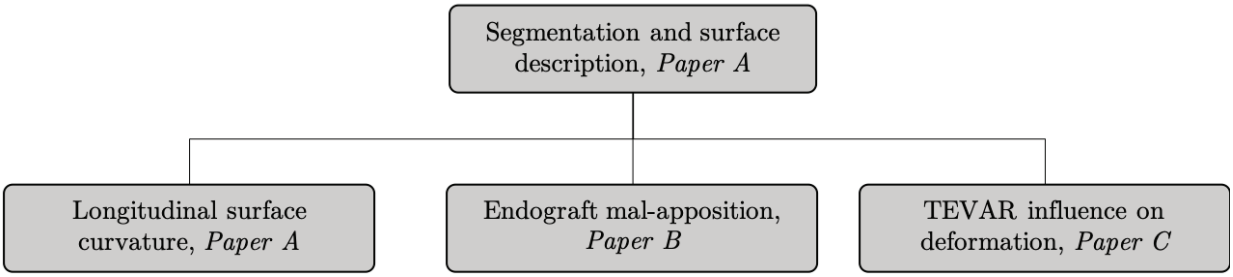

Figure 1.3: Figure showing a schematic overview of the relationship between conducted research and appended papers in this thesis. By establishing the methodology framework for segmentation and surface description, studies on applications can be performed.

1.2 Anatomy, Pathology, and Interventions

1.2.1 Thoracic Aortic Anatomy

The thoracic aorta is the most proximal segment of the human vasculature, originating from the aortic valve of the heart and ending when passing through the diaphragm, as seen in Figure 1.4. The thoracic aorta has three defined sub-segments; the *ascending aorta*, the *aortic arch*, and the *descending aorta*. The normal configuration of the thoracic aorta has three vessels branching off from the thoracic aortic arch, supplying the arms and head with oxygenated blood, in proximal order; *branchiocephalic artery (BA)*, *left common carotid artery (LCCA)*, and *left subclavian artery (LSA)* [11]. In addition to the arch branches, Figure 1.4 includes the *left* and *right coronary arteries*, which supply the heart with blood.

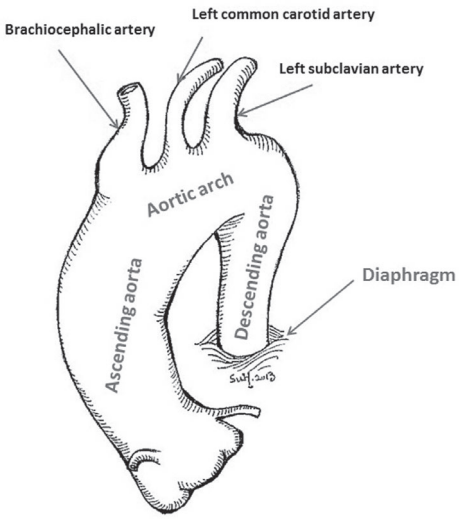

Figure 1.4: Figure showing an illustration of the thoracic aortic anatomy including branch vessels and segments. The left and right coronary arteries are seen close to the proximal end of the ascending aorta. Figure taken from [6].

1.2.2 Thoracic Aortic Pathology

As presented in the limitations section (1.1.2), the pathologies included in this thesis are thoracic aortic aneurysm and thoracic aortic dissection, see Figure 1.5. *Thoracic aortic aneurysm* is when the vessel wall is locally weakened and the cross-sectional diameter of the vessel is more than 50% larger than than normal. The dilation may grow over time, with an increasingly higher risk for rupture. Today the criterion for intervention is if the aneurysm diameter is larger than 5.5 cm or 6.5 cm for the ascending and descending thoracic aorta, respectively [12–14]. However, individual and more sophisticated criteria based on local rupture risk found by mechanical modeling of the vessel wall have been proposed [15–17]. Such methods could potentially be implemented. The treatment options are open surgical repair or endovascular repair. *Thoracic aortic dissection* occurs when blood leaks through a tear in the intima, the innermost layer of the vessel wall. The leakage is contained within the media, the middle layer, or in the interface between the media and adeventitia, the outermost layer, and this creates a parallel lumen called a false lumen, see Figure 1.5. The false lumen gets pressurized by the direct connection to main blood flow, and the pressure causes the original channel, the true lumen, to partially collapse decreasing the perfusion. The decreased perfusion may lead to ischemia, organ failure, or the damaged vessel wall may rupture. Treatments of dissections are either medical or through the same procedures as for aneurysms [13].

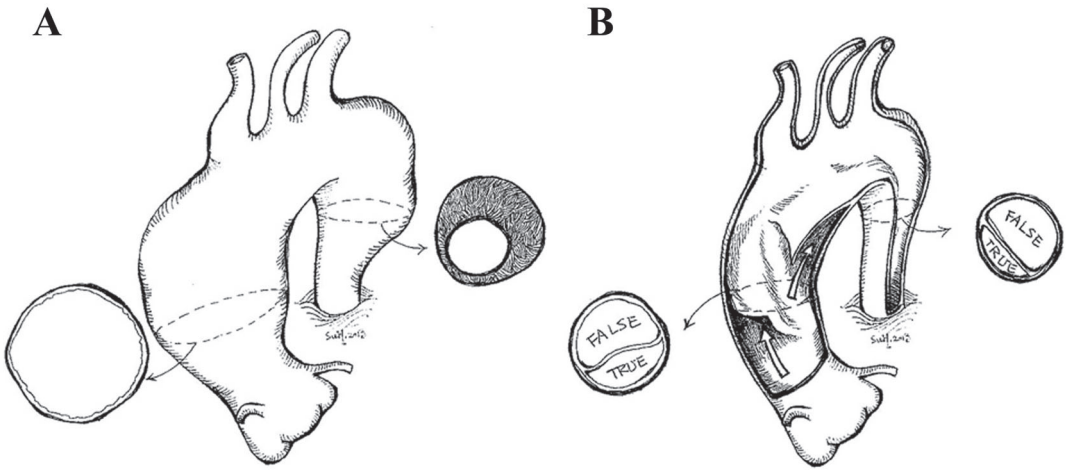

Figure 1.5: Figure showing illustrations of thoracic aortic pathologies, with thoracic aortic aneurysm of the whole thoracic aorta (A), and thoracic aortic type A dissection with an intimal tear in the ascending aorta (B). Figure taken from [6].

1.2.3 Endovascular Interventions and Devices

The previously presented diseases can be treated in different ways; medically, through open surgical repair, or endovascular intervention [18]. Within the limitations of this thesis, the procedural details and background are only further explained for TEVAR. Also, a brief description of *endografts*, the implant used in these interventions is presented.

Thoracic endovascular aortic repair is a minimally invasive intervention where access

to the vascular system is created through one or several punctures in the groins. For complex procedures, access to the vascular system may also be gained through the arms [18]. Guided by 2D x-ray imaging, the the vascular surgeon or interventional radiologist, navigates from the incision through the vascular system with guidewires to access the desired site of device deployment. The endograft is tightly folded into a small catheter and delivered endovascularly, hence the name. When the crimped endograft is at the correct location, it is deployed (*i.e.*, unfolded), creating an artificial vessel, see Figure 1.6a. Preoperatively, a computed tomography angiograpy (CTA) is performed to assist the clinician in selecting the right endograft (type and size) and to plan the intervention steps including identifying the most suitable location for deployment. The main advantages with these interventions are the ability to treat patients who would not be candidates for surgical open repair as well as a shorter recovery time and hospital stay [19, 20].

The implanted devices in these cases are endografts, an example is seen in Figure 1.6b. This artificial vessel is made from a tube of medical textile supported by a set of metal rings for radial stiffness. The most common types of textiles used are polyester and polytetrafluoroethylene (PTFE), and the metal rings are normally made from Nitinol. Nitinol is a super-elastic nickel-titanium alloy that allows crimping of the endograft into the delivery catheter (and large deformations *in-vivo*) without plastic damage [21]. The first endografts were introduced for treatment of human vessels in the early 1990s, and both devices and interventions have been improved significantly ever since [22, 23]. It is important that the improvement continues since both device and intervention-induced complications still occur. The advancements due to breakthroughs in different fields; improvements of the materials in the different endograft components give better durability, better imaging and modeling give better boundary conditions, and better tools for preoperative planning give better procedural outcomes.

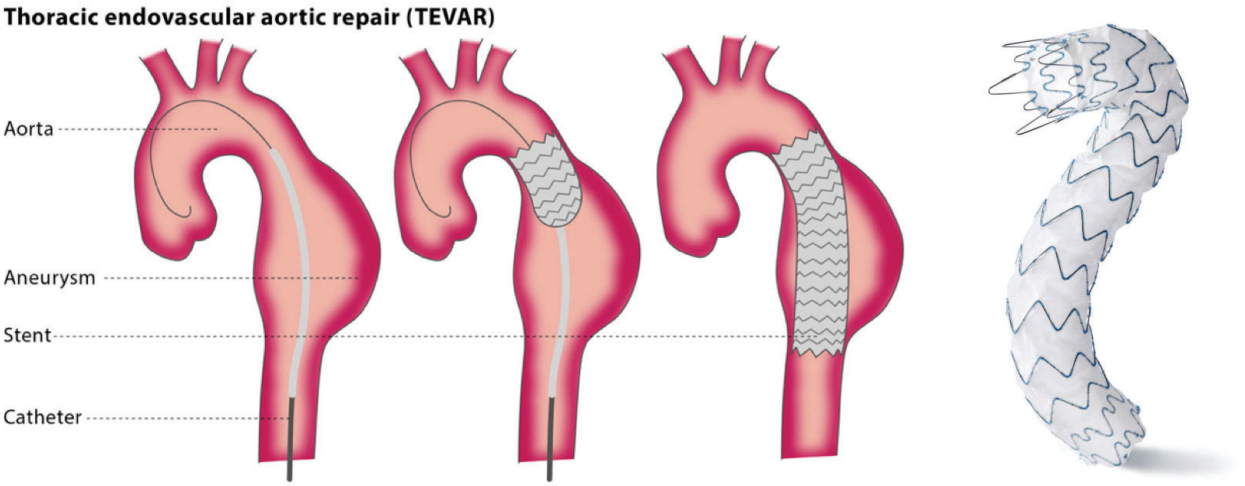

(a) Figure displaying the schematic steps of endograft deployment in the case of thoracic endovascular aortic repair of a thoracic aneurysm in the descending aorta. Figure taken from [14].

(b) Figure showing an endograft. Photograph from [24].

Figure 1.6: Figure showing the schematic steps of endograft implantation using thoracic endovascular aortic repair (a), and a photograph of an endograft (b).

2 Modeling of Aortic Surfaces

2.1 Imaging and modeling

Medical imaging gives the possibility to, non-invasively, visualize and describe internal anatomy and physiology. Over the years, several imaging modalities have been introduced, for example: radiation based (x-ray and positron emission tomography), ultrasound, and magnetic resonance imaging, to mention a few. The medical images used in this thesis are all from x-ray sources, namely CTA. Computed tomography (CT) creates a 3D-volumetric description of the body with high spatial resolution. This is achievable since the x-ray tube and the detector array on the other side of the object are allowed to rotate, and the examining table to translate. By rotating the source-detector pair a full 360° field of view can be created. By also moving the patient in the medial direction a cylindrical domain can be described. Angiography (the A in CTA) means that the target for the scanning is the vascular system, and to enhance the attenuation of the blood, contrast fluid (normally iodine for x-ray) is injected intravenously. When analysing the dynamics of the aortic surfaces, it is important to know at what time point during the cardiac cycle the image is acquired. To assure good accuracy here, the heart is monitored with an electrocardiograph and the images can then be extracted at the correct time point (prospective gating) or a continuous imaging sequence can be stored, and then sorted based on the cardiac cycle after the scan (retrospective gating).

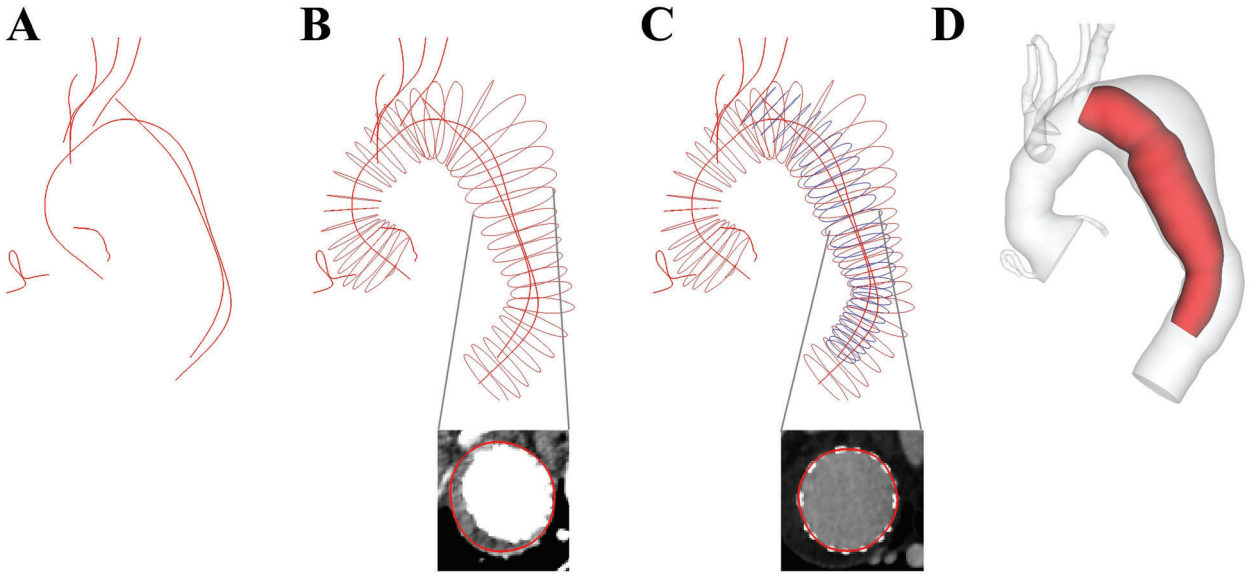

Figure 2.1: Figure presenting an overview of the steps used in the semi-manual modeling tool SimVascular. A shows 3D centerlines for a thoracic aorta, relevant branches and an endograft in the descending segment. B and C show 2D cross sections of the thoracic aorta and endograft, with examples from modeling of respective cross sections. D shows a rendering of lofted surfaces based on contours (intraluminal aortic surface in light grey, and endograft surface in red). Figure is taken from [6].

After the images have been acquired, they need to be modeled and segmented before quantification can be performed. Semi- and fully automatic methods for 3D segmentation are getting more and more common and in a few years, hopefully, the fully automatic methods can show satisfyingly good accuracy. As said, there are a lot of software options for handling the raw imaging files and in this project we have utilized SimVascular, which is an open source tool specifically developed for manual and semi-manual modeling and simulation of the vascular system [25]. The workflow is described in steps, as seen in Figure 2.1. First, the centerlines of the vessels and branches are hand-picked in the 3D volume (see Figure 2.1A). Second, following along these centerlines, 2D segmentation can be preformed at certain interval to capture the cross sections (see Figure 2.1B, and 2.1C). This is a natural way to describe a tubular structure and the result of this can then be lofted to a surface (see Figure 2.1D). Worth noting is that this needs to be repeated for every instant of time studied.

2.2 Segmentation

The labour intensive work of manual modeling can potentially be avoided, using an automatic segmentation algorithm. In **Paper A**, such an algorithm is presented and validated. It is dependent on a stereolithograpic (STL) surfaces as input and outputs a computational grid in the form of centerlines and 2D cross sections that are structured similarly to the output from SimVascular. In brief, the segmentation is mimicking the workflow of the manual process; creation of initial 3D centerline, cross section creation, form a new centerline, Fourier smoothing of new centerline, second-generation cross sections and then iteration of these steps to improve accuracy [26, 27]. The initial centerline is created using a custom made stepping algorithm minimizing the area of proxy-cross sections with varying orientation within the vessel, see Figure 2.2. One proxy cross plane at location $\boldsymbol{C}_i$ is defined with the the normal $\hat{\boldsymbol{\eta}}_i(\theta, \varphi)$, where the angles are varied: $\theta \in \left(\frac{-\pi}{2}, \frac{\pi}{2}\right)$ and $\varphi \in (0, \pi)$. The optimal plane orientation and contour at location i are found by minimizing the area of the contour, as described in Equation (2.1).

$$A_{\min,i} = \min_{\theta,\,\varphi} \int_0^{2\pi} \int_{C_i}^{\sigma_i(\theta,\varphi)} \mathrm{d}r\mathrm{d}\beta \tag{2.1}$$

where β is the circumferential direction, r is the radial direction, and θ and φ are the altitude and azimuth angles for the plane normal, as previously defined, respectively. The minimal area is found for a pair of optimized angles $\tilde{\theta}$ and $\tilde{\varphi}$, which gives the corresponding contour $\boldsymbol{\sigma}_i(\tilde{\theta}, \tilde{\varphi})$. The corresponding numerical algorithm uses the Shoelace formula to compute area. Starting at the proximal end of the STL-model, this procedure is repeated along the whole length by stepping distally. By connecting the centroids of the found contours, the initial 3D centerline is defined.

The details of the following iterative process are described in **paper A**. Multiple iterations of centerline forming, centerline smoothing and cross sectional contouring are performed. In some locations, the tortuousity and diameter of the aorta may cause adjacent cross sections to overlap intraluminally. At the end of each iteration, each set of contours is checked for overlap, and if present, the overlaps are pairwise fixed (by

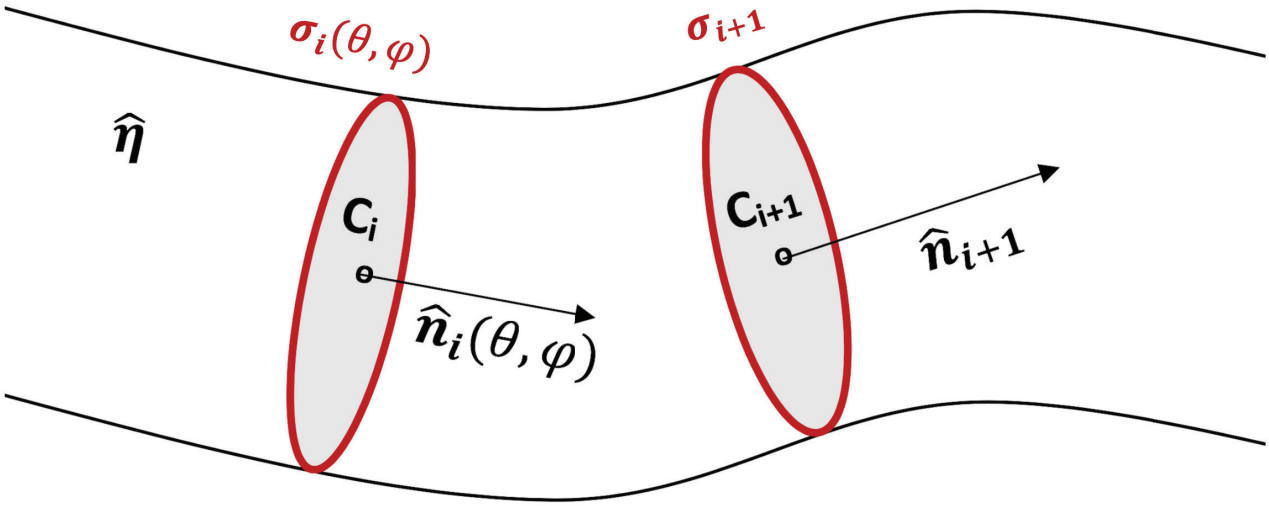

Figure 2.2: Visualization of two consecutive cross sections found to define the initial 3D centerline. $\boldsymbol{C}$ represent centroids and $\boldsymbol{\sigma}$ contours. $\hat{\boldsymbol{n}}$ and $\hat{\boldsymbol{\eta}}$ represents the contour, and surface normals, respectively. Using a stepping algorithm, the optimal cross sections are found along the whole length of the thoracic aorta. Figure is taken from **paper A**.

adjusting the pair of normals of the contours to relocate the intersection extraluminally), starting with the worst case of overlap within the set.

2.3 Lagrangian Formulation

Now, the surface geometries are defined, but to allow for dynamic comparisons and material point-wise tracking, the surface needs to be described in a Lagrangian cylindrical coordinate system. This natural description has previously been used in work by Fata, Smith and Lundh [28–30]. In this thesis, methods are based on Lundh [30]. The origin is defined at a bifurcation to a branch vessel, in this case, the LCCA, see Figure 2.3. Other markers at branches or, for example, at the location of endograft ends are useful for defining regions in the analysis. Fiducial markers, in addition to the LCCA, used in this thesis are; Right coronary ostium and BA to define the ascending aorta, BA and LSA to define the aortic arch, and LSA and the first intercostal artery to define the descending aorta. In **paper A** the whole thoracic aorta (ascending, arch and descending) is studied, whereas in **paper C** the ascending and descending segments are separately studied. For **paper C** markers for the endograft ends are used to define the stented region, specifically studied, see Figure 3.3. Finally, in **paper B** the proximal end of the endograft is of extra importance to define the bird-beaking metrics (see in Section 3.2). In **paper B** and **paper C**, the endograft end markers in relation to fiducial markers are used to determine the corresponding locations prior to intervention. For example, if the distal part of the endograft is situated 10 mm distal to the LCCA along the centerline arc-length postoperatively, the stented region is assumed to start 10 mm distal to the LCCA in the preoperative model as well.

Each material point on the surface is assigned a longitudinal and a circumferential

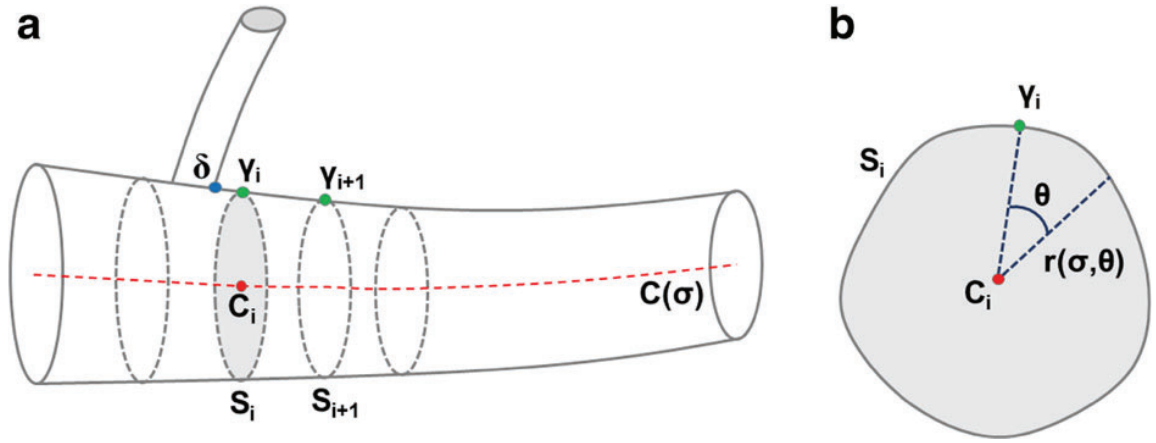

Figure 2.3: Figure showing a schematic description of the Lagrangian cylindrical coordinate system. A shows the longitudinal extent of the coordinate system. $\boldsymbol{\delta}$ marks the origin at a bifurcation of a branch, and based on this, the anatomical marker guideline formed by $\boldsymbol{Y}_1 ... \boldsymbol{Y}_i ... \boldsymbol{Y}_n$. $\boldsymbol{C}$ denotes the centroids and $\boldsymbol{S}$ the contours. B shows cross sectional view for contour i. $\boldsymbol{\sigma}$ and $\boldsymbol{\theta}$ are the longitudinal and circumferential positions, respectively. The figure is taken from [30].

index and could be viewed as a transformation, from a surface in 3D Cartesian coordinates to a 2D cylindrical coordinate system, when the radii are expressed as a function of σ and θ, as seen in Figure 2.3. The grid is built using linear interpolation based on the input contours and centerline and longitudinal and circumferential resolution can be set depending on needs. For example, to be able to compare a geometry point-wise between two time instances the two models need to have the same resolution. This is an inherent assumption; that the grid interval will be slightly stretched from one configuration to another if the surface is stretched, and that this stretch is equally distributed along the whole length and circumference, respectively.

3 Applications

3.1 Surface Curvature

A natural application for the Lagrangian grid is to quantify surface curvature explicitly for each point on the surface. In this case, in the circumferential and longitudinal directions, respectively. These can be used to compute mean and Gaussian curvature, which have been shown to be related to abdominal aortic aneurysm rupture risk [15, 31]. However, in this thesis, the focus is on longitudinal surface curvature, how it can be accurately quantified and in particular why it is important.

The general formula for curvature reads

$$\kappa = \frac{\|\mathbf{r}'(t) \times \mathbf{r}''(t)\|}{\|\mathbf{r}'(t)\|^3}, \tag{3.1}$$

where $\boldsymbol{r} = \boldsymbol{r}(t)$ is the parametric equation for the curve and primes refer to derivatives with respect to the parameter t. The curvature formula in Equation (3.1) is in this thesis discretized with a circle fitting method ($\kappa = \frac{1}{R}$, where R is the radius of curvature), which allows for implementation of a sliding window, to reduce noise. The optimal window size was suggested by Choi and Lundh [27, 30], respectively. Inspired by the circle fitting method, a straightforward method for estimating longitudinal surface curvature from centerline curvature and radii is also investigated. In this study the inner and outer lines are found in the following way; relying on the Lagrangian grid, the inner line is found as the shortest path between the levels of the right coronary artery and the intercostal artery fiducial markers, parallel to the anatomic marker guideline (see $\boldsymbol{Y}_1 ... \boldsymbol{Y}_i ... \boldsymbol{Y}_n$ in Figure 2.3). The outer line is chosen as the line 180° shifted from the inner line. The inner and outer local radii, based on points at the surface lines, are added to the inverse of centerline curvature at each point, yielding new radii of curvature. From these, the estimated inner and outer curvatures are computed, see Equations (3.2) and (3.3).

$$\kappa_{\text{outer, est}} = \frac{1}{\left(\frac{1}{\kappa_{\text{center}}} + r\right)} \quad \text{and} \tag{3.2}$$

$$\kappa_{\text{inner, est}} = \frac{1}{\left(\frac{1}{\kappa_{\text{center}}} - r\right)}, \tag{3.3}$$

where κ_{center} is the local centerline curvature and r is the local radius. $\kappa_{\text{outer, est}}$ and $\kappa_{\text{inner, est}}$ are the estimated curvatures for the outer line and inner line, respectively. The explicit surface curvature method correlates well with analytic solutions for longitudinal curvature for the defined inner and outer lines as well as for centerline curvature. The estimation method is working well for phantoms mimicking healthy vessels, but very poorly for those who represents diseased morphologies. An example of such poor performance can be seen in Figure 3.1. For patient geometries, this study confirms the hypothesis that the inner surface curvature is significantly higher than the centerline curvature, hence important to quantify in order to describe surface conditions accurately. The outer

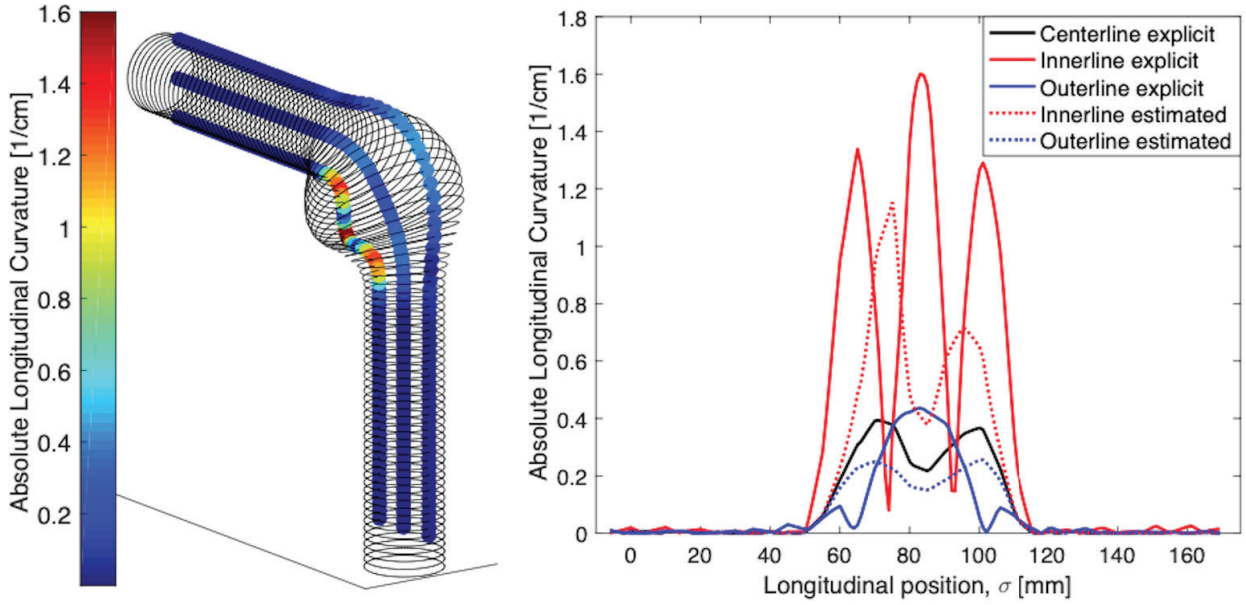

Figure 3.1: Figure shows explicit (point-wise quantified) longitudinal surface curvature along inner and outer lines for a computer generated phantom geometry (left), and comparison between explicit and estimated surface curvature along the length of the same phantom (right).

longitudinal surface curvature is not significantly different compared to the centerline curvature for the diseased thoracic aortas, a result that is expected for healthy vessels. This is explained by the influence of aneurysms and dissections, which cause local high areas of surface curvature, even on the outer curve.

3.2 Endograft Malapposition Prediction

By relying on the methods for imaging and modeling described in section 2.1, thoracic aortic and endograft surface models are constructed and forms the input for this application. The methodology for finding the inner line is in this case slightly modified compared to the surface curvature case. Instead of finding the shortest parallel line to the anatomic marker guideline, the center of mass (COM) for the thoracic aortic model located axially above the right coronary artery is defined. By minimizing the distance of all points on the most proximal contour to the COM, the starting point of the inner line is defined. This point is then projected onto the distal contours to form the full inner line using the same method as when defining the anatomic marker guideline based on the LCCA ostium, previously described. The inner line of the endograft is then found as the shortest distance to the aortic inner line, for each endograft contour at a time. After defined, the curves are smoothed using Fourier smoothing [27]. Based on these two curves, the longitudinal region of interest is defined from the point-pair g_0 (proximal end of the endograft) and a_0 (proximal landing point) to the distal point-pair g_1 and a_1 (where the threshold distance between the two curves drops below 3 mm), as seen in Figure 3.2. Bird-beak height (BBH)

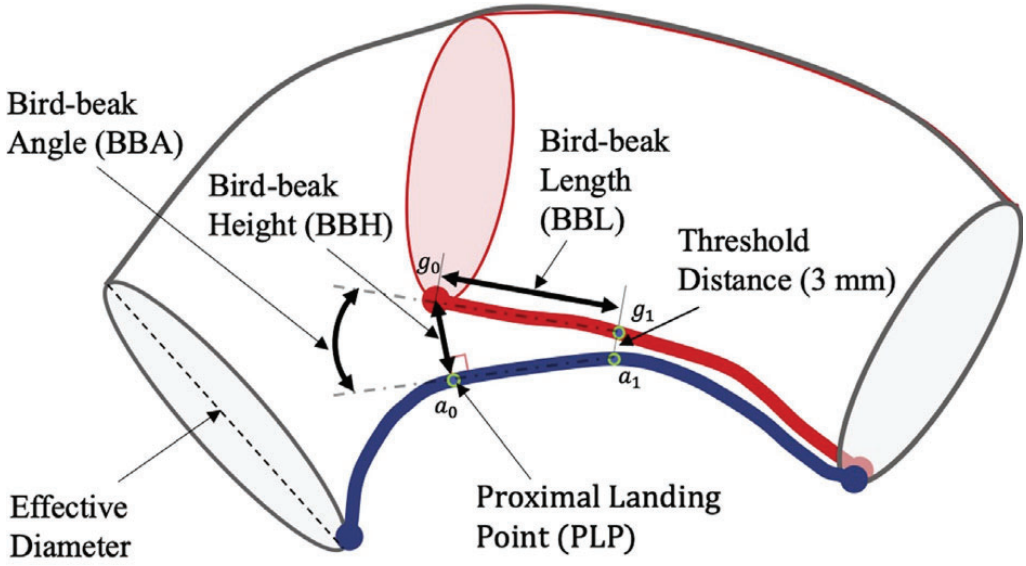

Figure 3.2: Figure displays a segment of the thoracic aorta around the proximal landing zone of the endograft. Bird-beak metrics including bird-beak angle, bird-beak height, and bird-beak length as well as the four points that underlies theses metrics a_0, a_1, g_0, and g_1, are visualized. Figure taken from **Paper B**.

was defined as the distance between g_0 and a_0, bird-beak length (BBL) as the Euclidean distance between g_0 and g_1, and finally the bird-beak angle (BBA) according to Equation (3.4).

$$BBA = \cos^{-1}\left(\frac{\mathbf{a}\cdot\mathbf{g}}{\|\mathbf{a}\|\|\mathbf{g}\|}\right), \tag{3.4}$$

where $\mathbf{a}$ is the vector between a_1 and a_0, and $\mathbf{g}$ is the vector between g_1 and g_0. Preoperatively, the inner surface curvature (quantified using the circle fitting method as described in Section 3.1) as well as the aortic effective diameter was measured at the proximal landing point, a_0. The effective diameter is calculated as

$$D_{\text{effective}} = 2\cdot\sqrt{\frac{Area}{\pi}}, \tag{3.5}$$

where $D_{\text{effective}}$ is the effective diameter and $Area$ is the cross-sectional area. For a fully circular cross-section the effective diameter is the same as the diameter. However, in the case of non-circular cross-sections, the effective diameter is different from the diameter since every point on the parameter has different radii, but it serves as a measure proportional to mean diameter. The level of local over-sizing is determined from this by comparing to the specifications of the endograft. In general, an over-sizing in the interval of 10% to 20% is recommended for these interventions and too much over-sizing (<30%) can be negative with regards to device migration [4, 32].

Using the inner surface curvature and the effective diameter, the unit-less product is found. The rationale for defining such a dimensionless metric is based on how tubes are constrained in bending. The inner curve needs to shorten, and the outer lengthen

to fulfil being perpendicular to the centerline. When the outer curve of the endograft is stretched fully, the inner curve cannot contract/wrinkle to accommodate for high inner surface curvature, bird-beaking occurs. With this said, this metric preop is significantly higher in cases of high bird-beaking postop. Also, this metric, along with the inner surface curvature alone, are found to correlate with both BBH and BBA, where the latter agrees with previous findings from Kudo *et al.* [33].

3.3 Multiaxial Deformation Changes Due to TEVAR

The third application to the presented framework is a study on multiaxial deformation of the thoracic aortic aorta. Models of thoracic aortas are constructed at ten different time-points during the cardiac cycle using retrospective gating, as described in Section 2.1. This is preformed for each of the eleven patients, both before and after TEVAR, yielding a total of 20 models per patient. The models are then defined in an Lagrangian cylindrical coordinate system (Section 2.3) to be able to quantify longitudinal surface curvature in the same way as presented in Section 3.1, and effective diameter as described in Section 3.2. These metrics are then extracted and studied in different segments, as described in Section 2.3 and further visualized in Figure 3.3. These methods give a set of metrics to assess how TEVAR affects the cardiac-induced deformation of the different segments of the thoracic aorta, and the results confirms the hypothesis that the stented portion exhibits a decrease in cardiac-induced deformation from pre- to postop. The stiffening of this segment affects the non-stented segment, where deformations increases locally.

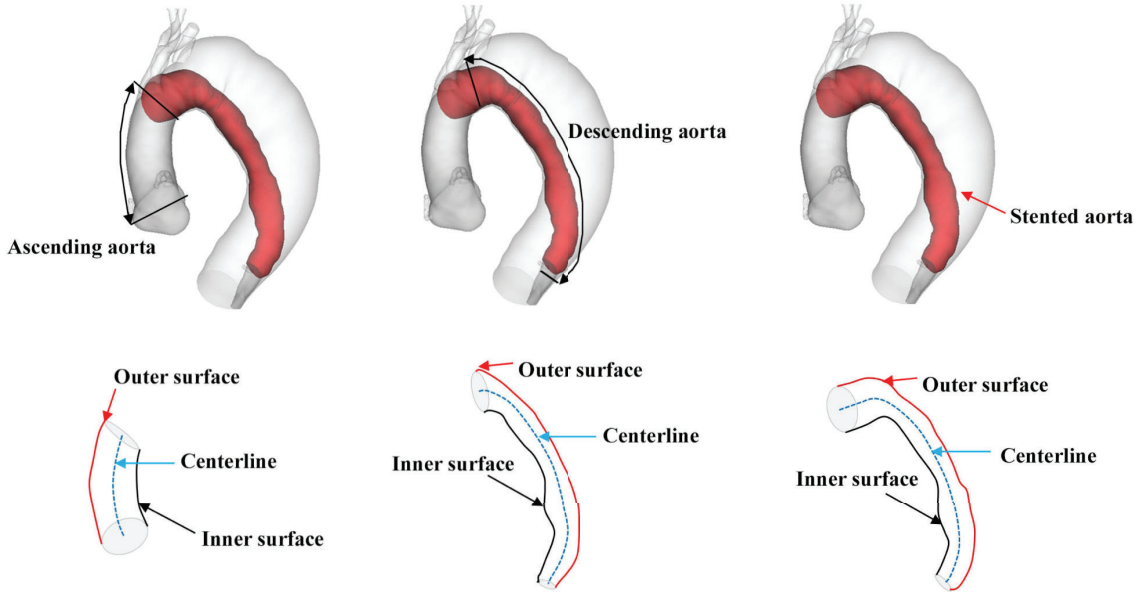

Figure 3.3: Figure showing the definition of inner, center and outer surface lines for the different segments studied in **paper C**. Light grey is the aortic intraluminal surface, dark grey is the true lumen surface, and the red is the endograft surface. The figure is modified from **paper C**.

4 Summary of Appended Papers

Paper A: Automated Quantification of Diseased Thoracic Aortic Longitudinal Centerline and Surface Curvatures
In this paper the automated segmentation algorithm and modeling framework were developed and validated on computer generated phantoms. This included automatic contouring of stereolithographic surfaces and then description in a Lagrangian cylindrical coordinate system. After validation, the algorithms were used to segment and quantify longitudinal surface curvature of 37 human thoracic aortas with aneurysm or dissection. The results confirmed hypotheses that the longitudinal surface curvature is significantly different for the longitudinal curvature of the centerline. It was also concluded that surface curvature cannot be approximated using a straightforward estimation method, especially not in the case of diseased thoracic aortas.

Paper B: Thoracic Aortic Geometry Correlates With Endograft Bird-Beaking Severity
In this paper methods for prediction of endograft malappositon based on pre-op data were developed. Analyses were then conducted on a cohort of 20 patients who had their aneurysms or type B dissection treated with TEVAR. By establishing metrics for bird-beak height, the cohort could be categorized into two subgroups; ten patients with, and ten patients without bird-beak occurrence. For the group where bird-beak configuration was observed, analyses of the preop- surfaces showed significant correlation between inner surface curvature and inner surface curvature·diameter with bird-beak height and bird-beak angle. It was also found that the product inner surface curvature·diameter was significantly higher for this group compared to the group that did not show bird-beaking postoperatively.

Paper C: Biomechanical Effects of TEVAR on Multiaxial Pulsatility and Surface Curvature Deformation of the Thoracic Aorta
In this paper an investigation on how the multiaxial deformation induced by cardiac motion is altered by TEVAR was carried out. The methods include modeling of ten cardiac frames for the thoracic aorta of eleven patients, before and after TEVAR and a set of quantities were extracted. Based on cross-sectional data, effective diameters could be measured, from the centerline, arclength and longitudinal curvature, and from the surfaces, inner and outer surface curvatures. Based on this, the cardiac induced arclength deformation was found to increase for the ascending aorta, but decrease for the stented aorta from pre- to post-TEVAR. The stented aorta also showed a decrease in outer surface curvature and diametric change. Hypothesised stiffening of the stented aorta was confirmed and the results indicate that this also affects the deformation of the ascending aorta.

5 Concluding Remarks and Future Work

5.1 Conclusions

In conclusion, an automatic tool for segmentation and quantification of surface metrics for thoracic aortas was developed, validated and used for explicit surface curvature computation. Advantages of the method are the possibility to extract additional metrics, and that several time-points can be compared by tracking material points. Inner surface curvatures are significantly different from centerline curvatures and this makes a crucial difference when describing boundary conditions for endografts, which are placed on the vessel walls. Explicit inner surface description and cross-sectional measurements have shown to be useful metrics for a predictive method for preoperative insight on optimal landing zones to avoid device malapposition. Finally, the effects of TEVAR on multiaxial pulsatility and surface curvature deformation have shown stiffening effects, *i.e.*, decreased deformation, in the stented segment, with a result in increased deformation for non-stented segments. The conclusion from this is that the influence of TEVAR may not just have a local influence, but rather altering the dynamic conditions for the whole thoracic aorta.

In essence, the work in this thesis has contributed to the two fundamental purposes of the project; It has given insight into device movement and provided more realistic boundary conditions for device manufactures, and assisted clinicians to better understand aspects of diseases and how vascular anatomies are affected by TEVAR. This altogether can potentially improve the durability of devices and the outcome of interventions — and ultimately the quality of life of treated patients.

5.2 Future Work and Preliminary Results

There are several direct continuations and broadening of the applications to **papers A-C**. Building on **paper A** a study of dynamic surface curvature for the whole surface could be conducted to complement the presented work in **paper C**. For **paper B**, we predict future work by expanding the number of patients and investigating devices from different manufacturers, and also how *active control*-delivery systems affect the bird-beaking issue. A proposed future work based on **paper C** is to conduct a larger cohort study with focus on aortic remodeling after TEVAR, possibly even with monitored blood pressure, mainly to study hemodynamic effects. A visualization of the relationship between presented and future work for these studies can be seen in the left bottom part of Figure 5.1. Additionally, the methodology presented in **paper A** is believed to be a good foundation for further customization and combination of metrics, depending on clinical – or biomechanical – hypotheses. In fact, such a project has already been initiated with focus on pathology and pathophysiology of Stanford type B dissections in general, and on modeling of the true and false lumen in particular. This utilizes a modified version of the segmentation tool and the Lagrangian coordinate system to define the longitudinal propagation of the true lumen by introducing the new metrics *helical angle* and *helicity*. Initial results were presented at the Transcatheter Cardiovascular Therapeutics-conference in September 2019

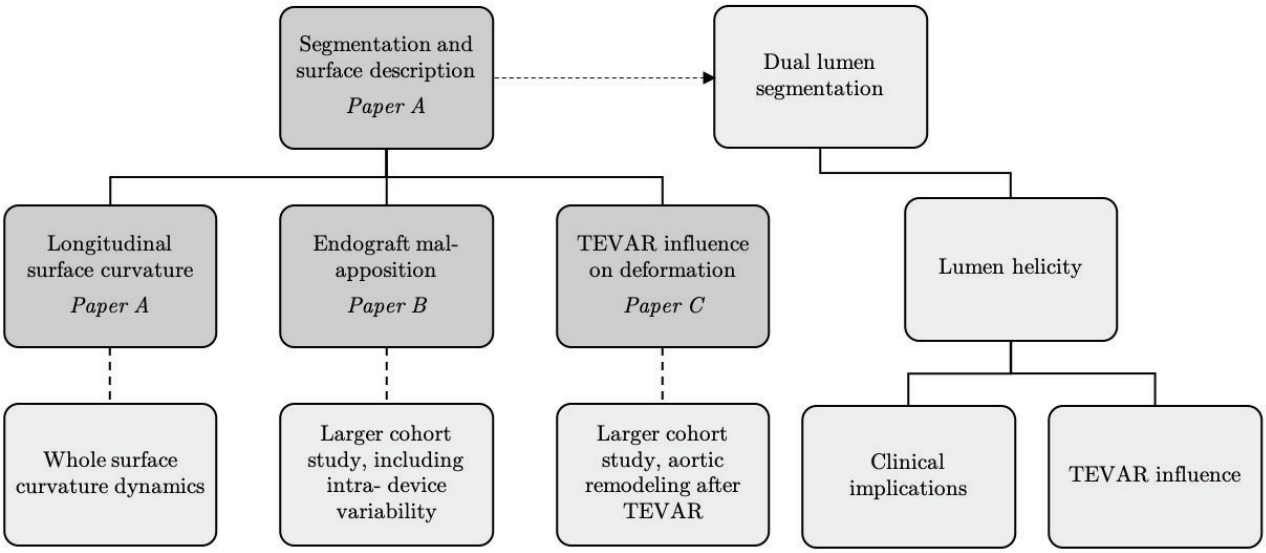

Figure 5.1: Figure showing a schematic Overview of the relationship between research in thesis (dark grey) and proposed future projects (light grey), *cf.* Figure 1.3.

and a summary of the method and results for one example patient are seen in Figure 5.2. In short, the true and aortic lumens of 19 patients were segmented simultaneously, and considering the level of helical angle, they clustered into two distinct groups; either with no helical angle, or a helical angle around -180°.

The initial results spark a set of interesting research questions:

- Would the helical angle of patients in a bigger cohort also cluster into these two distinct groups?
- Why are all true lumens (and therefore also false lumens) in the helical group propagating in the same direction?
- From a pathogenic standpoint; why are some propagating helically, and some not?
- How can we model the true and false lumen interaction?
- What factors play a role in the pathogeneis and etiology of type B dissections?
- How does interventions such as TEVAR affect lumen helicity?

These research questions are a part of the right branch in Figure 5.1, in addition to the earlier mentioned future work linearly linked to **papers A-C**, respectively.

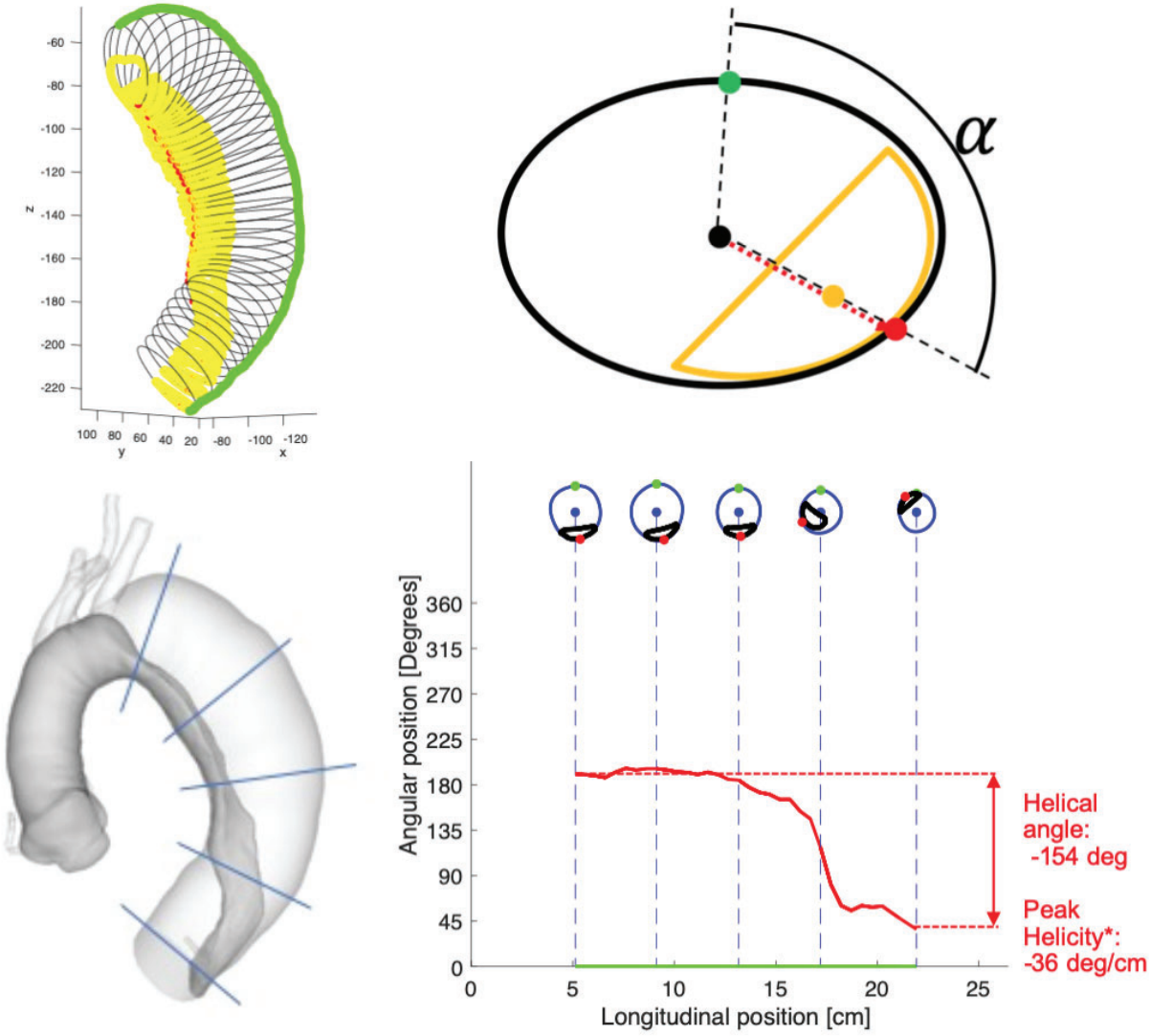

Figure 5.2: Figure shows a summary of future work in the right branch of Figure 5.1. Dual lumen segmentation (top left), definition of helical angle (top right), STL-surfaces for an example patient with five longitudinal locations (dark grey is true lumen, light grey is the false lumen), and helical angle and helicity varying along the dissected segment (bottom) are displayed.

References

[1] World Health Organization. *Cardiovascular diseases*. 2020. URL: https://www.who.int/health-topics/cardiovascular-diseases/#tab=tab_1 (visited on 01/27/2020).

[2] Takuya Ueda, Dominik Fleischmann, Michael D. Dake, Geoffrey D. Rubin, and Daniel Y. Sze. "Incomplete Endograft Apposition to the Aortic Arch: Bird-Beak Configuration Increases Risk of Endoleak Formation after Thoracic Endovascular Aortic Repair". *Radiology* 255.2 (2010), pp. 645–652. DOI: https://doi.org/10.1148/radiol.10091468.

[3] Yoshiaki Katada, Shunichi Kondo, Eitoshi Tsuboi, Ken Nakamura, Kyu Rokkaku, and Yoshihito Irie. "Type IA endoleak embolization after TEVAR via direct transthoracic puncture". *Japanese Journal of Radiology* 33.3 (2015), pp. 169–172. DOI: 10.1007/s11604-015-0392-7.

[4] W Charles Sternbergh 3rd, Samuel R. Money, Roy K. Greenberg, Timothy A. M. Chuter, and Zenith Investigators. "Influence of Endograft Oversizing on Device Migration, Endoleak, Aneurysm Shrinkage, and Aortic Neck Dilation: Results From the Zenith Multicenter Trial". *Journal of Vascular Surgery* 39.1 (2004), pp. 20–26. DOI: 10.1016/j.jvs.2003.09.022.

[5] Markus G.M. Steinbauer, Alexander Stehr, Karin Pfister, Thomas Herold, Niels Zorger, Ingolf Töpel, Christian Paetzel, and Piotr M. Kasprzak. "Endovascular repair of proximal endograft collapse after treatment for thoracic aortic disease". *Journal of Vascular Surgery* 43.3 (2006), pp. 609–612. DOI: 10.1016/j.jvs.2005.11.045.

[6] Christopher P. Cheng. *Handbook of Vascular Motion*. Academic Press, an Elsevier imprint, 2019. ISBN: 978-0-12-815713-8.

[7] Tikva S. Jacobs, Jamie Won, Edwin C. Gravereaux, Peter L. Faries, Nicholas Morrissey, Victoria J. Teodorescu, Larry H. Hollier, and Michael L. Marin. "Mechanical failure of prosthetic human implants: A 10-year experience with aortic stent graft devices". *Journal of Vascular Surgery* 37.1 (2003), pp. 16–26. DOI: 10.1067/mva.2003.58.

[8] The Mayo Clinic. *CT-scanner*. 2020. URL: https://www.mayoclinic.org/tests-procedures/ct-scan/about/pac-20393675 (visited on 02/10/2020).

[9] Arkansas Society of Radiologic Technologists. *Cath lab*. 2020. URL: https://www.arsrt.org/cath_lab.html (visited on 02/10/2020).

[10] Craig Bonsignore. *Open Stent Design*. Nitinol Devices & Components (NDC). 2020. URL: https://github.com/cbonsig/open-stent (visited on 02/10/2020).

[11] Gerald J. Tortora and Barry Derrickson. *Principles of Anatomy and Physiology*. 13th ed. Wiley, 2013. ISBN: ES8-1-118-34500-9.

[12] John A. Elefteriades. "Natural History of Thoracic Aortic Aneurysms: Indications for Surgery, and Surgical Versus Nonsurgical Risks". *The Annals of Thoracic Surgery* 74.5 (2002), pp. 1877–1880. DOI: 10.1016/s0003-4975(02)04147-4.

[13] David S. Strayer and Emanuel Rubin. *Rubin's Pathology. Clinicopathologic Foundations of Medicine*. 7th ed. LWW, 2014. ISBN: 978-1451183900.

[14] CIRSE. *Thoracic endovascular aortic repair(TEVAR)*. 2020. URL: https://www.cirse.org/patients/ir-procedures/thoracic-endovascular-aortic-repair-tevar/ (visited on 02/10/2020).

[15] Sergio Ruiz de Galarreta, Aitor Cazón, Raúl Antón, and Ender A. Finol. "The Relationship Between Surface Curvature and Abdominal Aortic Aneurysm Wall Stress". *European Journal of Cardio-Thoracic Surgery* 139.8 (2017), pp. 718–724. DOI: 10.1115/1.4036826.

[16] Christian T. Gasser. "Biomechanical Rupture Risk Assessment: A Consistent and Objective Decision-Making Tool for Abdominal Aortic Aneurysm Patients". *AORTA (Stamford)* 4.2 (2018), pp. 42–60. DOI: 10.12945/j.aorta.2015.15.030.

[17] Judy Shum, Giampaolo Martufi, Elena Di Martino, Christopher B. Washington, Joseph Grisafi, Satish C. Muluk, and Ender A. Finol. "Quantitative Assessment of Abdominal Aortic Aneurysm Geometry". *Annals of Biomedical Engineering* 39.1 (2011), pp. 277–286. DOI: 10.1007/s10439-012-0691-4.

[18] Fabrizio Fanelli and Michael D. Dake. "Standard of Practice for the Endovascular Treatment of Thoracic Aortic Aneurysms and Type B Dissections". *CardioVascular and Interventional Radiology* 32 (2009), pp. 849–860. DOI: 10.1007/s00270-009-9668-6.

[19] Christoph A. Nienaber, Natzi Sakalihasan, Rachel E. Clough, Mohamed Abouk-oura, Enrico Mancuso, James S. M. Yeh, Jean-Olivier Defraigne, Nick Cheshire, Ulrich Peter Rosendahl, Cesare Quarto, and John Pepper. "Thoracic endovascular aortic repair (TEVAR) in proximal (type A) aortic dissection: Ready for a broader application?" *The Journal of Thoracic and Cardiovascular Surgery* 153.3 (2018), pp. 3–22. DOI: 10.1016/j.jtcvs.2016.07.078.

[20] Thomas Franz. *Cardiovascular and Cardiac Therapeutic Devices*. Springer, 2014. ISBN: 978-3-642-53836-0.

[21] Thomas W. Duerig, Alan R. Pelton, and Dieter Stöckel. "An overview of nitinol medical applications". *Materials Science and Engineering* 273-275 (1999), pp. 149–160. DOI: 10.1016/S0921-5093(99)00294-4.

[22] Michael D. Dake, D. Craig Miller, Charles P. Semba, R. Scott Mitchell, Philip J. Walker, and Robert P. Liddell. "Transluminal Placement of Endovascular Stent-Grafts for the Treatment of Descending Thoracic Aortic Aneurysms". *New England Journal of Medicine* 331.26 (1994), pp. 1729–1734. DOI: 10.1056/NEJM199412293312601.

[23] Juan C. Parodi. "Endoluminal Treatment of Arterial Diseases Using a Stent-Graft Combination: Reflections 20 Years after the Initial Concept". *Journal of Vascular Surgery* 37.4 (1997), pp. 3–4. DOI: 10.1177/152660289700400102.

[24] Vascular News. *CryoLife receives CE mark for E-nya thoracic stent graft*. 2020. URL: https://vascularnews.com/cryolife-receives-ce-mark-for-e-nya-thoracic-stent-graft/ (visited on 02/04/2020).

[25] Nathan Wilson, Kenneth Wang, Robert W. Dutton, and Charles Taylor. "A Software Framework for Creating Patient Specific Geometric Models From Medical Imaging Data for Simulation Based Medical Planning of Vascular Surgery". *Medical Image Computing and Computer-Assisted Intervention, Lecture Notes in Computer Science* 2208 (2001). DOI: 10.1007/3-540-45468-3_54.

[26] Christopher P. Cheng, Yufei D. Zhu, and Ga-Young Suh. "Optimization of three-dimensional modeling for geometric precision and efficiency for healthy and diseased aortas". *Computer Methods in Biomechanics and Biomedical Engineering* 21.1 (2018), pp. 65–74. DOI: 10.1080/10255842.2017.1423291.

[27] Gilwoo Choi, Christopher P. Cheng, Nathan M. Wilson, and Charles A. Taylor. "Methods for quantifying three-dimensional deformation of arteries due to pulsatile and nonpulsatile forces: implications for the design of stents and stent grafts". *Annals of Biomedical Engineering* 37.1 (2009), pp. 14–33. DOI: 10.1007/s10439-008-9590-0.

[28] Bahar Fata, Danielle Gottlieb, John E. Mayer, and Michael S. Sacks. "Estimated in Vivo Postnatal Surface Growth Patterns of the Ovine Main Pulmonary Artery and Ascending Aorta". *Journal of Biomechanical Engineering* 135.7 (2013), pp. 71010–71012. DOI: 10.1115/1.4024619.

[29] David B. Smith, Michael S. Sacks, David A. Vorp, and Michael Thornton. "Surface Geometric Analysis of Anatomic Structures Using Biquintic Finite Element Interpolation". *Annals of Biomechanical Engineering* 28.6 (2000), pp. 598–611. DOI: 10.1114/1.1306342.

[30] Torbjörn Lundh, Ga-Young Suh, Phillip DiGiacomo, and Christopher Cheng. "A Lagrangian cylindrical coordinate system for characterizing dynamic surface geometry of tubular anatomic structures". *Medical and Biological Engineering and Computing* 56.9 (2018), pp. 1659–1668. DOI: 10.1007/s11517-018-1801-8.

[31] Kibaek Lee, Junjun Zhu, Judy Shum, Yongjie Zhang, Satish C. Muluk, Ankur Chandra, Mark K. Eskandari, and Ender A. Finol. "Surface Curvature as a Classifier of Abdominal Aortic Aneurysms: A Comparative Analysis". *Annals of Biomedical Engineering* 41.3 (2013), pp. 562–576. DOI: 10.1007/s10439-012-0691-4.

[32] Joffrey van Prehn, Felix J.V. Schlösser, Bart E. Muhs, Hence J.M.Verhagen, Frans L. Moll, and Joost A. van Herwaarden. "Oversizing of Aortic Stent Grafts for Abdominal Aneurysm Repair: A Systematic Review of the Benefits and Risks". *European Journal of Vascular and Endovascular Surgery* 38.1 (2009), pp. 42–53. DOI: 10.1016/j.ejvs.2009.03.025.

[33] Tomoaki Kudo, Toru Kuratani, Kazuo Shimamura, Tomohiko Sakamoto, Keiwa Kin, Kenta Masada, Takayuki Shijo, Kei Torikai, Koichi Maeda, and Yoshiki Sawa. "Type 1a endoleak following Zine 1 and Zone 2 thoracic endovascular aortic repair: effect of bird-beak configuration". *European Journal of Cardio-Thoracic Surgery* 52.4 (2017), pp. 718–724. DOI: 10.1093/ejcts/ezx254.